


Article

Insight into the Role of Cerium (III) Addition to a MgAl-LDH Coating on AA6082

Michele Fedel  and Michele Zampiccoli

Department of Industrial Engineering, University of Trento, Via Sommarive, 9, 38123 Trento, Italy;
michele.zampiccoli@alumni.unitn.it

* Correspondence: michele.fedel@unitn.it

Featured Application: Corrosion protection of aluminium alloys.

Abstract: In this work, Ce doped MgAl-LDHs layers have been developed through an in-situ synthesis method on 6082 aluminum surface. The aim was to gain mechanistic insight into the role of Ce(III) as an active corrosion inhibitor embedded in the LDHs layer. The development of the LDH structure was verified by checking the presence of the characteristic XRD peaks, the platelet morphology (evaluated by SEM-EDXS) and the functional groups (by FTIR-ATR analyses). The same techniques were employed to assess the effect of a prolonged immersion time in 0.1 NaCl on the Ce doped MgAl-LDH coatings. Electrochemical impedance spectroscopy (EIS) was employed to monitor the evolution of the electrochemical properties of the coatings during prolonged immersion in saline solutions. The findings suggest a crystallization/dissolution/precipitation mechanism which implies: (i) the formation of crystalline cerium compounds, such as $\text{Ce}(\text{OH})_3$, in the LDH structure during the synthesis; (ii) the dissolution upon exposure to the NaCl solution, thus leading to cerium ions release; (iii) the precipitation of amorphous Ce oxides/hydroxides at the cathodic sites when the metal starts to corrode; (iv), the consequent mitigation of the electrochemical activity of the metal and, thus, the reduction of the extent of corrosion.

Keywords: MgAl-LDH; AA6082; Ce doping



Citation: Fedel, M.; Zampiccoli, M. Insight into the Role of Cerium (III) Addition to a MgAl-LDH Coating on AA6082. *Appl. Sci.* **2021**, *11*, 8252. <https://doi.org/10.3390/app11178252>

Academic Editor: Chiara Soffritti

Received: 29 July 2021

Accepted: 25 August 2021

Published: 6 September 2021

Publisher's Note: MDPI stays neutral with regard to jurisdictional claims in published maps and institutional affiliations.



Copyright: © 2021 by the authors. Licensee MDPI, Basel, Switzerland. This article is an open access article distributed under the terms and conditions of the Creative Commons Attribution (CC BY) license (<https://creativecommons.org/licenses/by/4.0/>).

1. Introduction

Chromate conversion coatings (CCC) have been widely used as anticorrosive treatments for zinc, steel, and aluminum alloys until 2006 [1–3] thanks to the undeniable active corrosion protection (ACP) provided by Cr(VI) species. However, the European directive 2002/95/CE [4] banned the use of chromium for anticorrosive surface finishing due to the high toxicity to human health and due to environmental impact of Cr(VI) on living species [5]. In the last decades, numerous studies have been aimed towards the substitution of Cr(VI) based surface conversion treatments for corrosion protection purposes. In particular, hexafluorozirconic acid (H_2ZrF_6) [6–13] and hexafluorotitanic acid (H_2TiF_6) [14–16] based treatments, silicon alkoxides derived sol-gel coatings [17–20], Cr(III) conversion treatments [21–23], and lanthanides based conversion coatings [24–26] gained prominent attention.

As far as lanthanides based conversion treatments are concerned, cerium salts proved to be able to provide a certain active healing effect if properly released in correspondence of a corrosion site [27,28]. The exploitation of the inhibition properties of cerium dates back to the mid-1980. Eco-friendly cerium compounds-based conversion films are recognized to provide corrosion mitigation through a cathodic inhibition effect [29,30].

In addition to the well-established surface conversion treatments, recently, a new class of talc-based coatings (namely layered double hydroxides, LDHs) has also been deeply investigated as a promising surface finishing for corrosion protection purposes.

LDHs are hydrotalcite-like clays (generally termed as anionic clays) constituted by lamellar hydroxides (Figure 1) typically having two types of metallic cations arranged in octahedral sites forming a layered crystalline structure [31,32]. The overall positively charged layers are electrically counterbalanced by interlayer water molecules and anionic species [33,34]. The general formula of an LDH is expressed as $[M_{1-x}^{2+}M_x^{3+}(\text{OH})_2]^{q+} (X^{n-})_{q/n} \cdot m\text{H}_2\text{O}$ where M^{2+} and M^{3+} are divalent and trivalent metal cations, respectively, x stands for the molar ratio $M^{2+} / (M^{2+} + M^{3+})$ and X^{n-} represents an anion having charge n^- [35]. Usually, the divalent and trivalent metal cations are Mg^{2+} , Zn^{2+} , Cu^{2+} , Mn^{2+} , Co^{2+} , Al^{3+} , Cr^{3+} and Fe^{3+} ions but also lanthanides and bismuth, having comparable ionic radii, can isomorphically substitute the trivalent metallic cations [36]. For what concern the inter-domain anions, F^- , Cl^- , Br^- , I^- , oxides as NO_3^- , CO_3^{2-} , sulfates and chromates or more complex organic and inorganic compounds can be present as counterbalancing species. Generally, anions having high charge density are preferentially intercalated into the LDH complex [37–39]. According to the recent reviews on this topic [40,41], several LDH based coatings were developed by the in-situ method on aluminum alloys and were demonstrated to provide the substrate with improved corrosion protection. The anti-corrosion properties of these compounds are recognized to rely on two factors: (i) the ion-exchange mechanism through which corrosive species as chlorides are entrapped into the LDH structure, being thermodynamically more favored than other species to lay inside the domains [42,43], and (ii) a physical barrier effect that protects the substrate [44,45]. Rare earth elements (in particular, lanthanum) have been successfully employed to modify LDH coatings either synthesized by means of the co-precipitation method [46,47] and synthesized in situ on aluminum alloys [48–51]. In a previous work devoted to Ce(III)-doped MgAl-LDHs layers developed on anodized AA6082 [52], we observed a beneficial effect in terms of improved durability provided by the presence of cerium ions. However, the role of cerium was not investigated in-depth, and the corrosion protection mechanism was only hypothesized. In this work, we aim at gaining mechanistic insight into the role of Ce(III) as an active corrosion inhibitor embedded in the LDHs layer. For this reason, we performed the deposition of Ce doped MgAl-LDHs layers by the in-situ method on AA6082. The synthesis time was varied to assess the potential of the synthesis route to embed the lanthanide ions in the LDH structure. The structural and chemical properties and the morphological features of the LDHs layers were evaluated prior and after the exposure to a saline containing environment to investigate the role of the cerium on the corrosion processes occurring on the metal surface. The evolution of the surface conditions during the exposure was monitored by means of electrochemical impedance spectroscopy (EIS). The investigation of the surface of the samples after the exposure to the aggressive solution, along with the electrochemical assessment, revealed an active role of cerium to mitigate the corrosion process occurring on the metal surface.

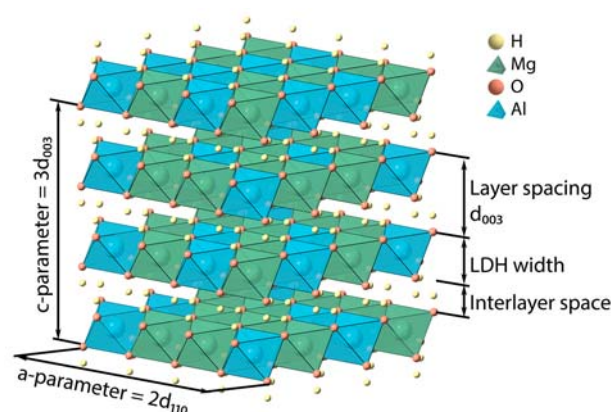


Figure 1. Schematic illustration of a MgAl-LDH.

2. Experimental Section

2.1. Materials

The samples were obtained from a laminated AA6082 T6 aluminum plate (wt.%; 0.70–1.30 silicon, 0.50 iron, 0.10 copper, 0.40–1.00 manganese, 0.60–1.20 magnesium, 0.25 chromium, 0.20 zinc, 0.10 titanium, and balance aluminum) provided by Metal Center S.r.l. (Italy) having a thickness equal to 3 mm. The samples were degreased by sonication for 6 min in acetone. To remove impurities and the near-surface deformed layer (NSDL), a chemical pickling into a 5 wt.% NaOH solution of for 6 min and a desmutting in a 30 wt.% HNO₃ solution was performed. The specimens were rinsed with DI water after each treatment.

2.2. Synthesis of Mg-Al Layered Double Hydroxide

The MgCe-LDH coatings were developed in situ employing a solution containing 0.01 M Mg(NO₃)₂ · 6H₂O, 0.06 M NH₄NO₃, and 0.001 M Ce(NO₃)₂ · 6H₂O. To get a complete overview of the effect of the synthesis parameters, different pH (6, 8, and 10) and treatment times (1, 4.5, 9, 18, and 27 h) were investigated (not reported results). This preliminary investigation revealed that a pH ≥ 10 is needed to develop an LDH architecture on AA6082 fully. For synthesis time longer than 9 h, the competitive mechanism of formation/dissolution of LDHs was revealed to be detrimental for developing the brucite structure. Based on these preliminary results, only the samples immersed at a pH 10 from 1 to 9 h were considered and analyzed in-depth in the present study. The other synthesis parameters, such as the temperature and the solution's stirring speed, were kept constant at 80 °C and 350 rpm, respectively.

A simply pickled and desmuted AA6082 plate (named Blank throughout the manuscript) was kept as a reference. At the same time, the other samples were labelled using the “C” letter followed by the corresponding pH and treatment time. The desired pH was reached by dropwise addition of NH₄OH. At a pH of 10, the precipitation of Ce(OH)₃ occurs as expected [53,54], leading to the formation of a yellowish solution (Figure 2) [55]. All the chemicals were purchased from Sigma Aldrich (Burlington, MA, USA).

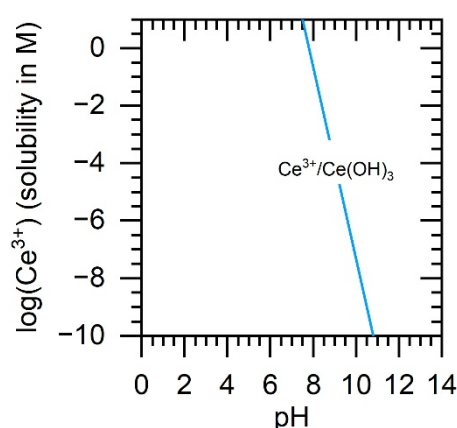


Figure 2. Equilibrium curves for Ce³⁺/Ce(OH)₃ as a function of the solution pH. The image is reproduced from [55].

2.3. Characterization

The electrochemical impedance spectroscopy measurements (EIS) were collected over a 1 cm² exposed area. The impedance curves were collected over 216 h into 0.1 M Na₂SO₄ + 0.05 M NaCl solution (23 ± 2 °C, pH 5.8). The reduced chloride content (0.05 M NaCl) allows to minimize the EIS data scattering in the low-frequency domain (<0.1 Hz). A Metrohm AutoLab PG Stat 302 N (Utrecht, The Netherlands) was employed. An amplitude of 10 mV (rms) and a frequency range from 10 mHz to 100 kHz were selected. The experimental EIS datasets were fitted using ZSimpWin software. A three-electrode cell

arrangement consisting of an Ag/AgCl reference electrode (3.5 M KCl, + 0.205 V vs. SHE), a platinum ring counter electrode, and the analyzed samples as a working electrode was employed. The morphology of the surface and the cross-section of the selected MgCe-LDHs were observed by an SEM (JEOL JSM-IT300, Tokyo, Japan) equipped with an energy dispersive spectrometer (EDS). The crystallographic structure was analyzed by XRD (X'Pert High Score diffractometer—Rigaku, Tokyo, Japan) with Cu emission source ($\lambda = 1.54056 \text{ \AA}$), the monochromator operating at 30 kV–10 mA and the scanning rate set at 4 min^{-1} . The LDH characteristic peaks reflections (hkl) were used to measure the basal space d_{hkl} and to evaluate the integral breadth β needed to calculate the crystallite size D by the Scherrer formula, Equation (1) [56]. The Scherrer constant K is assumed equal to 0.9 [57]. The lattice parameters a , b , and c were calculated by using Equation (2) related to the hexagonal crystal system, where d is the lattice spacing calculated by the Braggs law. The functional groups and the chemical bonding were investigated by FTIR-ATR (Varian 4100 FTIR Excalibur Series, Santa Clara, CA, USA) in the wavenumber range from 500 to 4000 cm^{-1} with a resolution of 4 cm^{-1} and acquiring 32 scans for each spectrum. All the analyses were performed on the as-synthesized materials and after 400 h of immersion in 0.1 NaCl solution. SEM images were also taken after the EIS measurement over 216 h.

$$D = \frac{K\lambda}{\beta \cos \theta} \quad (1)$$

$$\frac{1}{d^2} = \frac{4}{3} \left(h^2 + hk + \frac{k^2}{a^2} \right) + \frac{l^2}{c^2} \quad (2)$$

3. Results

ATR-FTIR was used to study the effect of prolonged immersion time (400 h) in 0.1 M NaCl ($23 \pm 2 \text{ }^\circ\text{C}$, pH 5.8) on the structural properties of the LDH coatings. The peaks assignment is performed considering the as prepared C10-9 sample in Figure 3, but it is the same for the other samples. The solid lines refer to the as-synthesized condition, the dashed lines to the samples immersed in 0.1 M NaCl during 400 h.

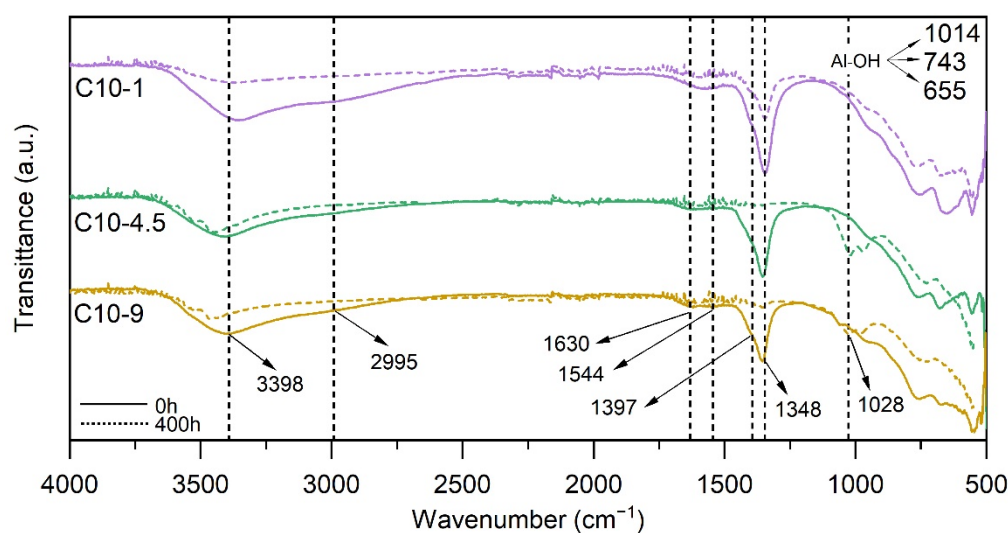


Figure 3. IR spectra from 500 cm^{-1} to 4000 cm^{-1} for C10 series obtained in ATR mode.

Between 3500 and 2750 cm^{-1} there is the characteristic absorption band of hydrotalcite given by the overlapping of two or even three OH stretching vibrations that belong to interlayer water molecules and hydroxides basal layer in the brucite-like structure $\text{Mg}(\text{OH})_2$ and $\text{Al}(\text{OH})_3$ [58]. At 2995 cm^{-1} it seems to be present a partially hidden peak, that in combination with the signal at 1544 cm^{-1} suggests the presence of asymmetric stretching of carbonate ions CO_3^{2-} [59]. The position of the peak at 3398 cm^{-1} found for the C10-9 is not

the same for the C10-1 sample as it is slightly shifted toward lower wavenumbers. Since the band position is inversely related to the bond strength of the cation to the oxygen ion [60], the shift could be related to the lower bond strength of the OH group to the divalent metal cations Mg^{2+} . On the other hand, for C10-9 specimen, the higher replacement of Mg^{2+} by Al^{3+} ions, which have higher charge and smaller radius, results in a stronger hydrogen bond between LDH layers. At 1630 cm^{-1} the peak can be associated with the bending vibration of water molecules present in the interlayer domain [61]. The signal at 1348 cm^{-1} can be attributed to the asymmetric stretching bond of CO_3^{2-} [62,63]. Nitrates and carbonates are intercalated between the brucite-like layers, and they are formed from the nitrate salt present in the initial synthesis solution and from CO_2 dissolved from the atmosphere. Absorption peaks of aluminum hydroxides Al-OH are found at 1014 , 743 , and 655 cm^{-1} while at lower wavenumber, between 540 and 650 cm^{-1} , there are the signals of Al-O and Mg-O groups. The peak at 1028 cm^{-1} is likely to be related to the NO_2^- group bonded to a metal cation (Mg^{2+} or Al^{3+}) through one of its oxygen atoms, forming the so-called nitro complexes [64]. Therefore, the peak under investigation can be attributed to the NO symmetric stretching, while the associated N=O stretching and the ONO bending vibrations are located at 1397 cm^{-1} and $825\text{--}830\text{ cm}^{-1}$, respectively. The broad signal in the high wavenumber range was investigated by analyzing the deconvolution of the FTIR spectra of the C10-4.5 sample (represented in Figure 4a). Four absorption bands are found in the region between 3750 and 2250 cm^{-1} . According to Figure 4a, the cyan broadband at 2995 cm^{-1} is associated with the vibration mode of water molecules and carbonate group that forms $\text{CO}_3^{2-} - \text{H}_2\text{O}$ bonds. It represents the major contribution to the overall peak since the integrated area is equal to 53%. The second blue peak at 3260 cm^{-1} is due to hydrogen-bond interlayer water. The third band, located at 3396 cm^{-1} , represents the second major contribution and it is given by the stretching mode of the M-OH bond. Moreover, the fourth peak is associated with the same hydroxyl vibration mode. Which metal is bonded with the OH or OH_2 is complex to determine since it depends on the LDH crystal structure, in particular, the $\text{M}^{2+}/\text{M}^{3+}$ ratio. Instead, at a higher wavenumber is more probable to have a signal related to $\text{Mg} - \text{OH}_2$ or $\text{Al} - \text{OH}_3$ [60].

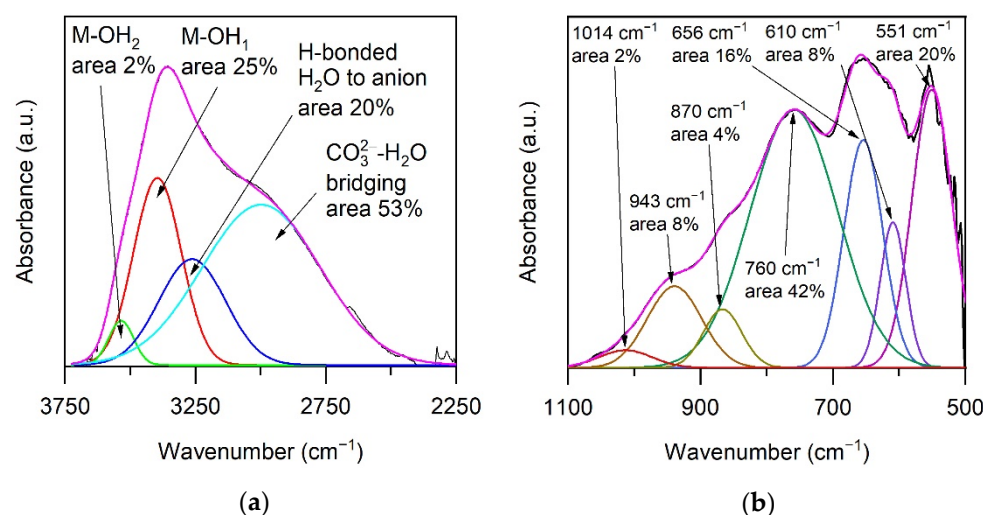


Figure 4. Deconvolution analysis of the ATR-FTIR spectra from (a) 3750 to 2750 cm^{-1} and (b) 1100 to 500 cm^{-1} of fresh sample C10-4.5. The Violet curve represents the sum of all deconvoluted signals. In black, the experimental curve.

A similar investigation on the deconvolution of the absorption band was done for the region between 1100 and 500 cm^{-1} (Figure 4b). The peaks located at 551 and 760 cm^{-1} are related to the translation modes of the hydroxyl group mainly attached to Al^{3+} . The associated deformation modes are represented by two signals at 943 and 1014 cm^{-1} . The absorption band found at 610 cm^{-1} is assigned to the hydroxyl translation modes attached

mainly to Mg^{2+} . The peaks at 656 and 870 cm^{-1} are attributed to the asymmetric stretching modes of the interlayer carbonate groups. The relative percentage of the different chemical groups were found not to differ significantly with synthesis time (from 1 to 9 h).

After the exposure in the electrolyte for 400 h, the lowering in peak intensity suggests the dissolution of the LDH coatings along with the release of ionic species. The peaks associated with the asymmetric stretching NO_3^- at 1348 cm^{-1} and the ONO bending vibration at 1397 cm^{-1} disappear for the C10-4.5 and C10-9 samples, thus suggesting the release of the nitrogen compounds as a result of the intercalation of Cl^- ions. The $\text{Cl}^- \leftrightarrow \text{NO}_3^-$ exchange is recognized to play a role in corrosion resistance as it is suggested that the nitrate-containing LDH coatings are effective nano-traps that can entrap chloride ions and, thus, postpone the initiation of the corrosion process [42]. Under the favorable conditions, the dissolved Mg^{2+} ions could form hydroxy compounds, $\text{Mg}(\text{OH})_2$, which can inhibit the spread of the pitting corrosion [65]. Interestingly, it is possible to observe the signal split at 1028 cm^{-1} observable in C10-1 and C10-9 spectra, which is attributed by some authors [63] to the symmetric stretching of the carbonate CO_3^{2-} . However, in this case the corresponding increase in the signal of both the symmetric and asymmetric stretching vibration of CO_3^{2-} at 1544 cm^{-1} is not observed.

Figure 5 shows the XRD patterns of the in situ developed LDH films. Between 10° and 45° , it is possible to observe the characteristic peaks of LDH that confirm the hydrotalcite layer's presence, in accordance with the FTIR results. They have miller indexes (003), (006), and (009) and they are located at 13 , 25.5 , and 40° , respectively [66]. Small signals are present at about 13 , 27 , and 32° that can be attributed to the formation of cerium hydroxide $\text{Ce}(\text{OH})_3$ or oxide CeO_2 [48,67]. The 2θ range between 45 and 65° was omitted since it contains only reflections belonging to the Al substrate and intermetallic particles [68]. In the 2θ range between 65 and 110° , the peaks at 72 and 73° are distinctive of the cell planes (110) and (113).

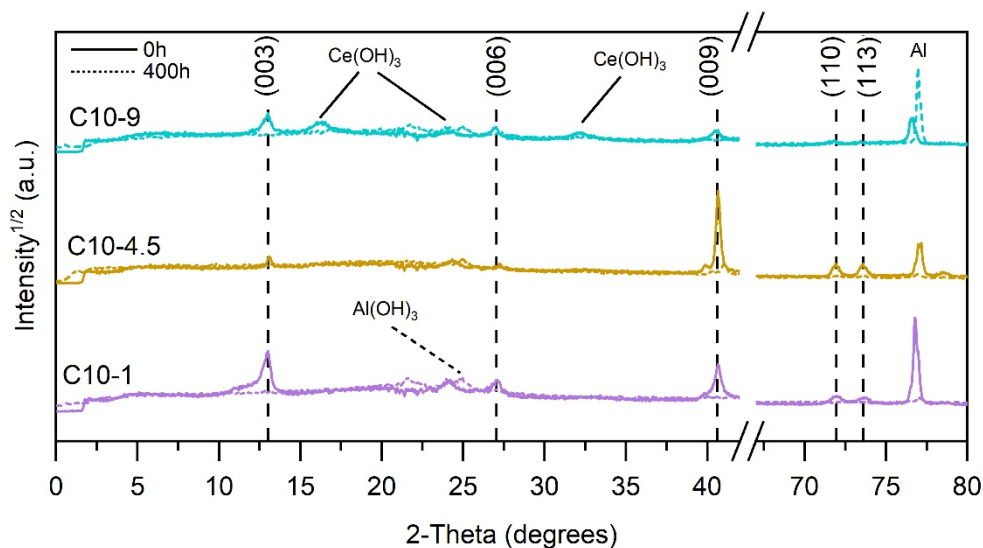


Figure 5. XRD pattern from 10° to 110° of C10 series C10 in their fresh state (solid lines) and after 400 h 0.1 M of NaCl immersion (dashed lines).

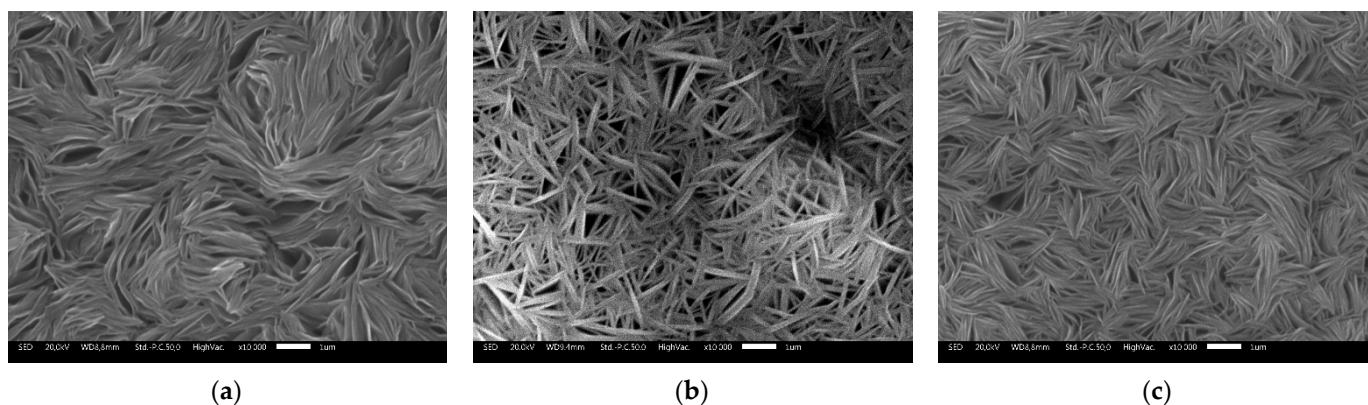
The d_{hkl} basal spacing and the crystal size D were calculated: the results are reported in Table 1. The FWHM parameter was used instead of the integral breath, and it was calculated by employing the OriginLab software. The reflection peak related to the plane (003) was used to measure $c = 3 \cdot d_{003}$ and the plane (001) for $a = 2 \cdot d_{110}$ [44].

Table 1. XRD analysis results: cell parameters *a* and *c* and crystallite size *D*. All values are expressed in nm.

Sample	Lattice Parameter		Interlayer Distance				Crystallite Size
	<i>a</i>	<i>c</i>	<i>d</i> ₀₀₃	<i>d</i> ₀₀₆	<i>d</i> ₀₀₉	<i>d</i> ₁₁₀	<i>D</i>
C10-1	0.2662	2.0591	0.6831	0.3294	0.2217	0.1311	2.9835
C10-4.5	0.2623	2.0261	0.6755	0.3271	0.2216	0.1312	5.5919
C10-9	0.2629	2.0464	0.6830	0.3307	0.2226	0.1315	2.8406

The XRD patterns collected after 400 h of immersion in 0.1 M NaCl are reported in Figure 5 as dashed lines. Looking at the low and high angle regions, it is clear that the signals belonging to the LDH structure have almost completely disappeared, thus suggesting the partial loss of crystallinity. The wide broad signal between 15 and 35° can be assigned to the aluminum hydroxide Al(OH)₃ formed as corrosion product after the chloride attack or to aluminum oxide Al₂O₃, as suggested by the search-match results made in the COD databases. The signals belonging to the crystalline cerium compounds at 15 and 17° disappeared, suggesting that they solubilize, releasing the cerium ions during the prolonged immersion.

According to the XRD results, the top-view of SEM images in Figure 6 highlights a well distinct platelet morphology, especially for C10-4.5 which shows the higher crystallinity (Figure 6b). For a shorter and longer treatment time, Figure 6a,c, the LDH nano-sheets seem to merge in a more refined and compact structure. The thickness of the different LDH layers was measured by SEM and was found to be 11.6 ± 1.3 µm, 5.1 ± 0.3 µm, and 9.8 ± 0.8 µm for the C10-1, 4.5, and 9 samples, respectively.

**Figure 6.** SEM images of the top-view of the as synthesized samples: (a) C10-1, (b) C10-4.5, and (c) C10-9.

In accordance with the XRD pattern, cerium-rich agglomerates, probably Ce(OH)₃, are found on the surface of the LDH coatings, (Figure 7), regardless of the synthesis time. The EDS map collected over the agglomerate in Figure 7a highlight the presence of Ce.

The appearance of the LDH coatings after 400 h of exposure to 0.1 M NaCl solution is reported in Figure 8a–c. Among the investigated LDH coatings, only the C10-4.5 structure still shows a platelet-like structure (Figure 8b), even if cracks are present over the surface. On the contrary, the LDH cannot be observed anymore in the samples C10-1 and C10-9 in Figure 8a,c seems that the LDH coating is completely dissolved.

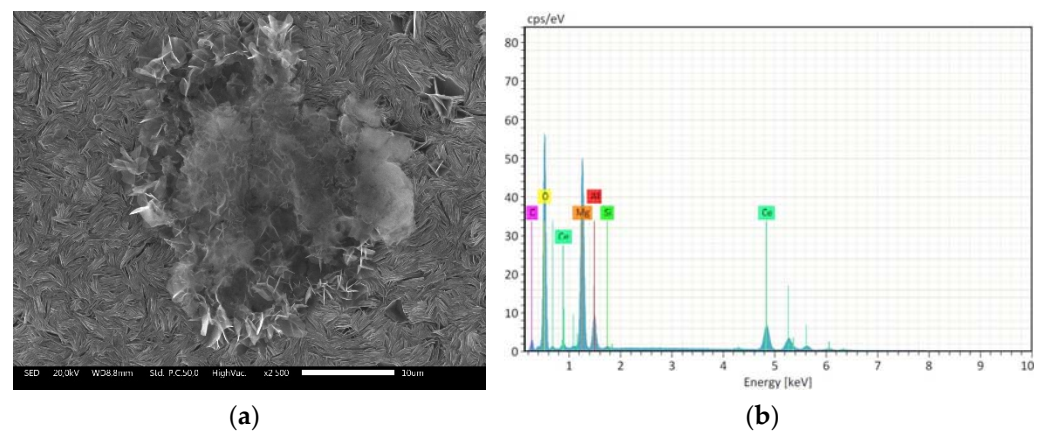


Figure 7. Ce-rich agglomerate on LDH surface (a) and the corresponding EDS analysis (b).

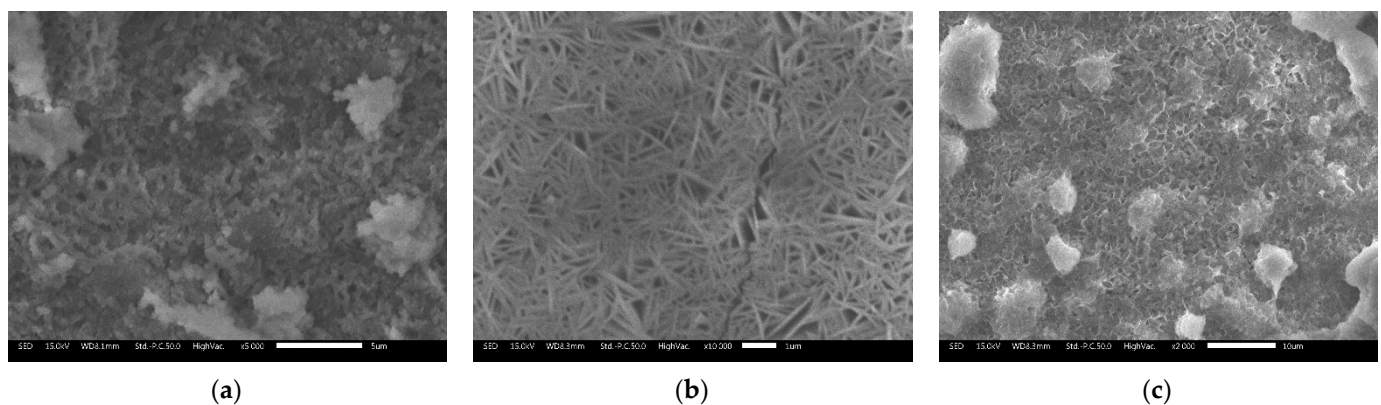


Figure 8. SEM images of the top-view of the investigated samples after 400 h of immersion in 0.1 M NaCl: (a) C10-1, (b) C10-4.5, and (c) C10-9.

By investigating the surface of the sample C10-4.5 (Figure 9) it is possible to observe different agglomerates: (i) platelet-like clusters whose main constituents are Al, Mg, and traces of zinc (Figure 9a); (ii) corrosion products consisting of Al hydroxides and alloying elements such as Fe, Mn, and Si (Figure 9b); and (iii) cerium-rich agglomerates (Figure 9c). The cerium-rich agglomerates are believed to be amorphous structures since no peaks corresponding to the crystalline form of Ce compounds were found in the XRD pattern after 400 h of immersion (Figure 5). We hypothesize that the crystalline structure such as $\text{Ce}(\text{OH})_3$ or CeO_2 formed during the synthesis in the LDH structure dissolves during exposure to the NaCl solution, thus releasing cerium ions. Gradually, the LDH layer cracks, and the corrosion of the substrate occurs. At the cathodic site, oxygen reduction leads to the formation of an alkaline environment, which promotes the precipitation of amorphous Ce oxides/hydroxides. These compounds are recognized to reduce the cathodic reaction rate, providing mitigation of electrochemical activity of the metal and, thus, reducing the extent of corrosion.

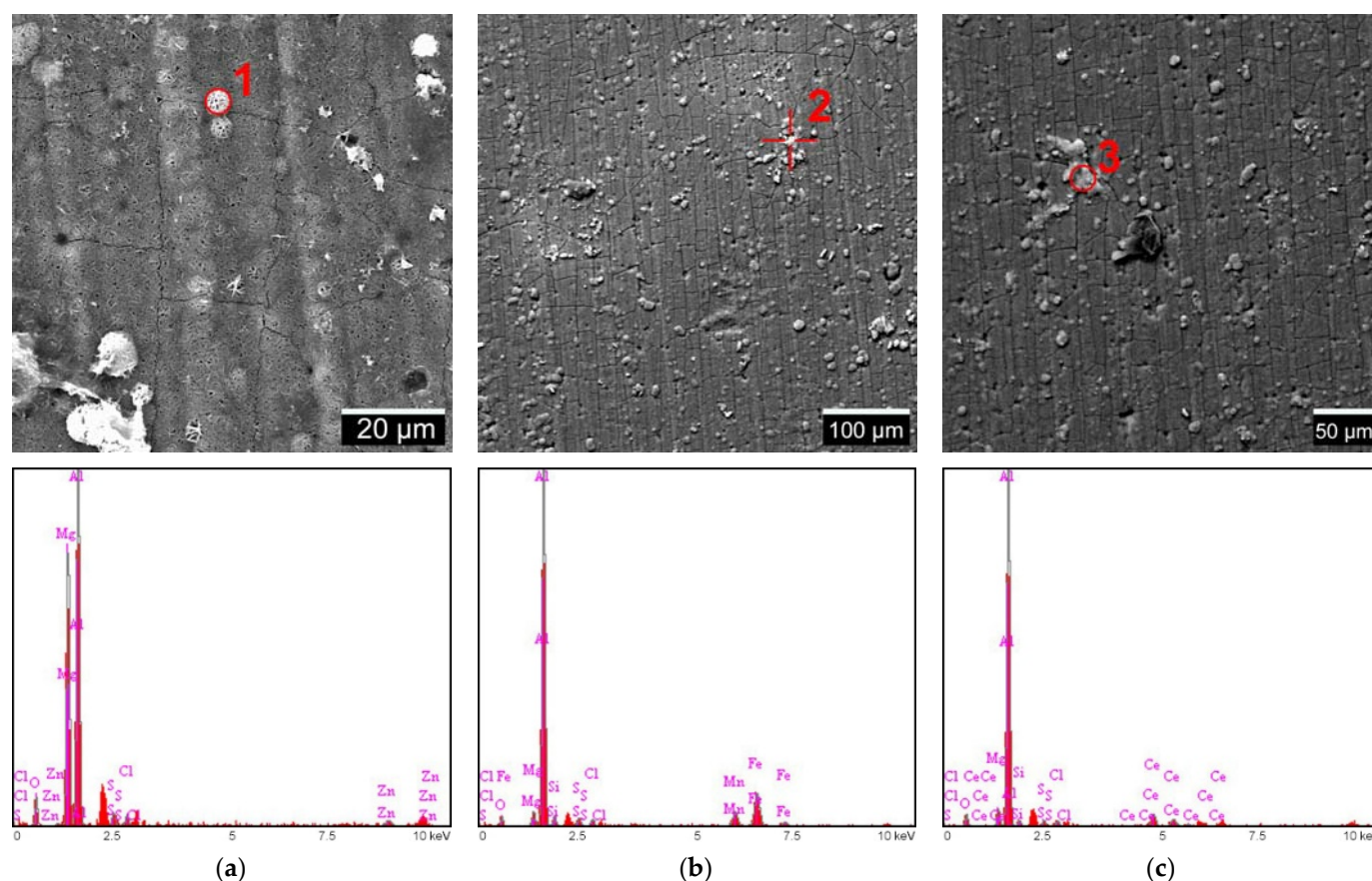


Figure 9. Three types of agglomerates found on C10-4.5 surface after 400 h of immersion in 0.1 M NaCl (a–c). At the bottom, the respective EDS analysis.

The effect of cerium in the LDH coating and its corrosion inhibition potential were better investigated by collecting EIS spectra in 0.05 M NaCl + 0.1 M Na₂SO₄ solution during 216 h. As explained in a previous section, the electrolyte was selected to reduce the electrochemical noise in the low-frequency range.

Figure 10 shows the impedance and phase diagrams of the investigated coatings during immersion time (2, 8, 24, 72, 168, and 216 h) in the electrolyte. Notice that the impedance modulus in the low-frequency range (about 0.01 Hz) shows an initial slight decrease in the very first hours of immersion and then a gradual increase with time elapsed. At the end of the immersion test (216th h), the C10-1 and C10-4.5 samples show impedance values higher than at the beginning. The observed trend is consistent with a sort of healing effect provided by the dissolution of cerium compounds, release of cerium ions, and precipitation of cerium oxides/hydroxides in correspondence of the cathodic sites on the metal surface, according to the previously discussed mechanism.

At an early stage of immersion, two-time constants can be observed in the middle-low frequency range. The relaxation processes tend to partially overlap for prolonged immersion time, as suggested by the merging of the phase angle peaks into a single asymmetrical peak. The time constant in the middle-frequency range is recognized to be related to the response of the LDH coating [69], while the attribution of the relaxation process in the low-frequency range is not straightforward. According to Zhu et al. [70] the low-frequency time constant derives from the superimposition of the contribution of the faradic process at the interface and that of the aluminum oxide. According to the previous description of the observed time constants, the experimental EIS datasets were fitted employing the circuit depicted in Figure 11. According to the $R_{sol}(Q_{LDH}(R_{LDH}(Q_{LF}R_{LF})))$ circuit in Figure 11, the equivalent electric parameters are defined as follows: R_{sol} stands for the solution resistance; R_{LDH} and the CPE_{LDH} are the resistance and the constant phase element associated with the

LDH coating [41,48,71,72]; the resistance R_{LF} in parallel with the constant phase element CPE_{LF} were employed to fit the relaxation process in the low-frequency range. Constant phase elements (CPE), were used instead of pure capacitance to account for surface inhomogeneity, fractal geometry, roughness, electrode porosity, and the current and potential distribution of the system surface [73]. Accordingly, $Z_{CPE} = 1/[Q(j\omega)^\alpha]$, where α is the frequency dispersion factor ($-1 < \alpha < 1$) the terms Q , j , and ω are the pre-exponential factor, the imaginary unit $j = \sqrt{-1}$, and the angular frequency, respectively.

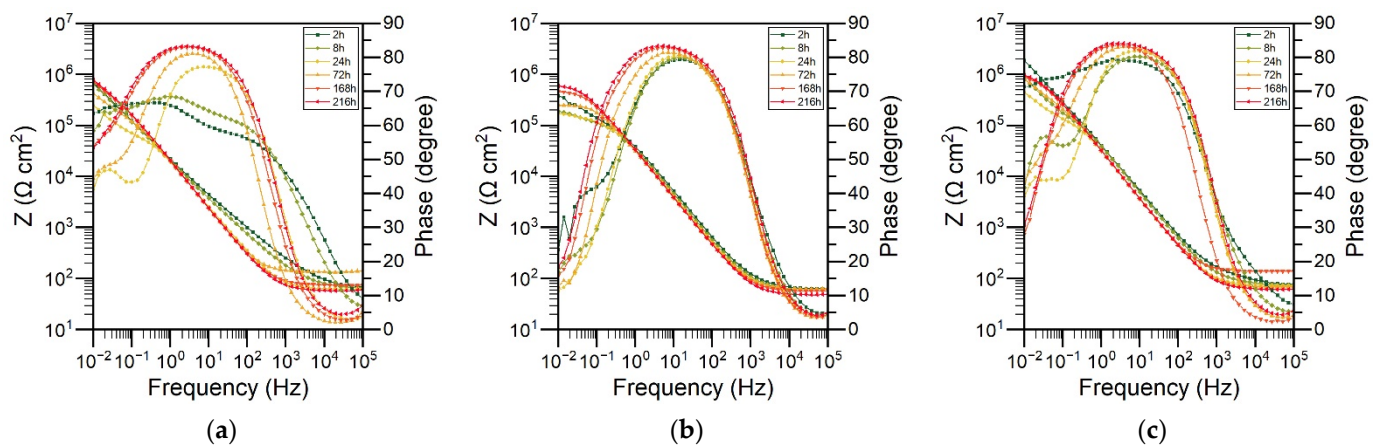


Figure 10. Impedance and phase angle plots of (a) C10-1, (b) C10-4.5, (c) C10-9 after 2, 8, 24, 72, 168, and 216 h of immersion.

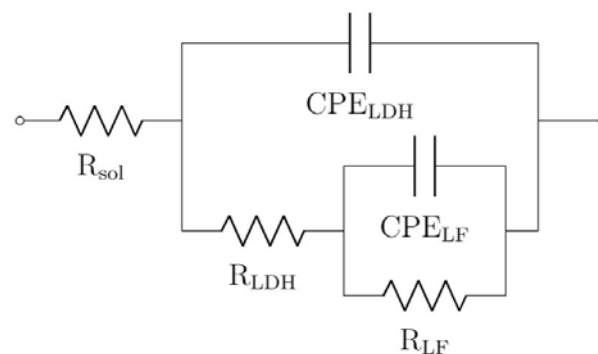


Figure 11. ECC used for curve fitting.

The results of the fitting are reported in Tables 2–4 for C10-1, 4.5, and 9, respectively. The values of the Q_{LDH} (pre-exponential factor of the CPE_{LDH}) are in the order of $10^{-6} \text{ S cm}^{-2} \text{ s}^\alpha$ regardless of the synthesis parameters. The corresponding α_{LDH} values are quite far from unity and, thus, a clear physical meaning cannot be attributed to the fitting parameter Q_{LDH} . Although Q_{LDH} is likely to reflect the dielectric properties of the LDH coating, due to the surface roughness, porosity, and corrosion products [74,75], the α_{LDH} values differ from unity. Thus, a comparison among the numerical values of the Q_{LDH} is not consistent. Similarly, for the values of the Q_{LF} (pre-exponential factor of the CPE_{LF}) it is not possible to define a clear physical meaning, as the α_{LF} values scatter from 0.67 to 1 throughout the immersion time. The values corresponding to the resistance R_{LDH} are quite scattered due to the partial porosity of the coatings [76].

Table 2. Results of EIS fitting for C10-1 sample.

Time [h]	R_{sol} [$\Omega \text{ cm}^2$]	CPE_{LDH} [$\text{S cm}^{-2} \text{ s}^\alpha$]	α_{LDH}	R_{LDH} [$\Omega \text{ cm}^2$]	CPE_{LF} [$\text{S cm}^{-2} \text{ s}^\alpha$]	α_{LF}	R_{LF} [$\Omega \text{ cm}^2$]
2	62.65	3.91×10^{-6}	0.73	2.74×10^3	8.86×10^{-6}	0.67	2.06×10^6
8	63.17	9.90×10^{-6}	0.75	2.65×10^3	1.66×10^{-6}	0.79	3.14×10^6
16	63.71	9.67×10^{-6}	0.84	1.18×10^5	4.17×10^{-5}	1.00	3.93×10^5
24	62.76	9.80×10^{-6}	0.89	9.14×10^4	4.63×10^{-5}	0.96	3.30×10^5
72	136.00	9.02×10^{-6}	0.93	2.21×10^5	2.49×10^{-5}	0.89	6.82×10^5
168	75.75	9.07×10^{-6}	0.92	6.85×10^5	1.70×10^{-5}	0.97	1.39×10^6
216	59.18	8.98×10^{-6}	0.92	8.32×10^5	1.94×10^{-5}	1.00	1.30×10^6

Table 3. Results of EIS fitting for C10-4.5 sample.

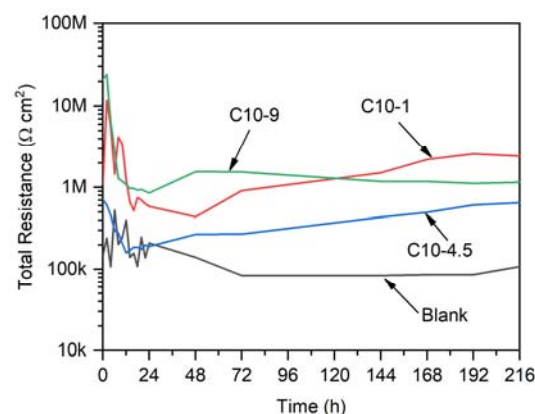
Time [h]	R_{sol} [$\Omega \text{ cm}^2$]	CPE_{LDH} [$\text{S cm}^{-2} \text{ s}^\alpha$]	α_{LDH}	R_{LDH} [$\Omega \text{ cm}^2$]	CPE_{LF} [$\text{S cm}^{-2} \text{ s}^\alpha$]	α_{LF}	R_{LF} [$\Omega \text{ cm}^2$]
2	65.89	4.84×10^{-6}	0.89	1.62×10^{-5}	2.14×10^{-5}	0.92	3.22×10^5
8	62.74	5.23×10^{-6}	0.90	1.28×10^5	6.82×10^{-5}	0.85	1.13×10^5
16	65.73	5.47×10^{-6}	0.90	1.35×10^5	1.63×10^{-4}	0.98	4.39×10^4
24	62.75	5.68×10^{-6}	0.91	1.37×10^5	9.58×10^{-5}	0.79	5.86×10^4
72	62.13	3.18×10^{-6}	0.96	1.78×10^2	2.78×10^{-6}	0.86	2.70×10^5
168	68.28	3.26×10^{-6}	0.96	1.81×10^2	2.41×10^{-6}	0.87	4.34×10^5
216	57.19	3.04×10^{-6}	0.96	1.54×10^2	2.60×10^{-6}	0.87	4.95×10^5

Table 4. Results of EIS fitting for C10-9 sample.

Time [h]	R_{sol} [$\Omega \text{ cm}^2$]	CPE_{LDH} [$\text{S cm}^{-2} \text{ s}^\alpha$]	α_{LDH}	R_{LDH} [$\Omega \text{ cm}^2$]	CPE_{LF} [$\text{S cm}^{-2} \text{ s}^\alpha$]	α_{LF}	R_{LF} [$\Omega \text{ cm}^2$]
2	73.76	3.58×10^{-6}	0.81	1.55×10^2	1.65×10^{-6}	0.95	1.59×10^7
8	79.09	5.06×10^{-6}	0.91	1.61×10^5	2.19×10^{-5}	1.00	6.55×10^5
16	80.31	5.37×10^{-6}	0.92	1.68×10^5	2.81×10^{-5}	0.97	5.58×10^5
24	75.60	5.69×10^{-6}	0.93	1.80×10^5	2.64×10^{-5}	0.95	5.40×10^5
72	70.09	5.82×10^{-6}	0.93	4.88×10^5	1.38×10^{-5}	0.94	9.81×10^5
168	140.00	2.64×10^{-6}	1.00	3.12×10^2	3.12×10^{-5}	0.85	1.07×10^6
216	61.31	2.22×10^{-6}	1.00	1.03×10^2	3.47×10^{-5}	0.88	1.17×10^6

According to the evolution with time of R_{LF} , an initial decrease of about one order of magnitude is observed in the first hours of immersion, followed by an increase at a later stage. This kind of behavior was observed for all the investigated samples.

To better investigate the evolution of the resistive behavior of the protection system, the evolution with time of the total resistance (given by the sum $R_{LDH} + R_{LF}$) was considered (Figure 12). The LDH dissolution is represented by the lowering of the curve in the first hours of immersion, precisely from 12 M $\Omega \text{ cm}^2$ to 520 k $\Omega \text{ cm}^2$ for C10-1, from 700 k $\Omega \text{ cm}^2$ to 160 k $\Omega \text{ cm}^2$ for C10-4.5, and from 24 M $\Omega \text{ cm}^2$ to 860 k $\Omega \text{ cm}^2$ for C10-9.

**Figure 12.** Evolution of the total resistance over 216 h of immersion.

The curve position of the C10-4.5 sample suggests the lower resistance against corrosion with respect to the other LDH treated during 1 and 9 h for the whole period of immersion but still much higher than the bare aluminum (sample named “Blank”), which remains stable at $100 \text{ k}\Omega \text{ cm}^2$. For all the treated samples, after 24–48 a recovery of the resistance value is observed, especially for the samples C10-1 and C10-4.5, while the C10-9 sample seems to maintain certain stability after days of immersion. According to the previously explained mechanism, this behavior was attributed to the dissolution, release, and precipitation of cerium compounds. This hypothesis is further supported by the presence of Ce-rich agglomerates (hydroxides or oxides) on the surface of the LDH coatings after 216 h of immersion in $0.05 \text{ M NaCl} + 0.1 \text{ M Na}_2\text{SO}_4$ (Figure 13).

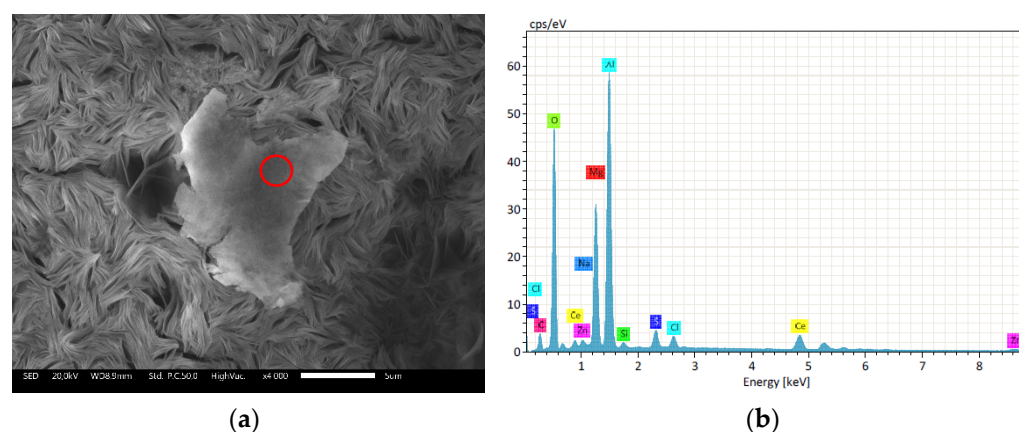


Figure 13. Ce-rich agglomerate on C10-1 surface after 226 h of immersion (a) and EDS analysis in correspondence of the red spot (b).

4. Conclusions

In this study, we aimed to gain mechanistic insight into the role of Ce(III) as an active corrosion inhibitor embedded in the LDHs layer. For this reason, we performed the deposition of Ce doped Mg-Al LDHs layers by the in-situ method on AA6082.

XRD and FT-IR measurements along with SEM images, collected before and after 400 h of continuous immersion in the 0.1 M NaCl solution, suggested a corrosion inhibition mechanism based on the dissolution and re-precipitation of Ce compounds. In particular:

1. Ce-based crystalline structures such as $\text{Ce}(\text{OH})_3$ or CeO_2 forms during the LDH in-situ synthesis;
2. Upon exposure to the NaCl solution, Ce-based structures dissolves (thus leading to cerium ions release), the LDH layer cracks and corrosion initiates;
3. At the cathodic sites, oxygen reduction leads to the formation of an alkaline environment, which promotes the precipitation of amorphous Ce oxides/hydroxides, reducing the cathodic reaction rate and providing mitigation of the corrosion rate of the metal.

The EIS investigation in the mild electrolyte ($0.1 \text{ M Na}_2\text{SO}_4 + 0.05 \text{ M NaCl}$ solution) further supports the proposed mechanism: the total resistance of the protection system shows an initial decrease in the first hours of immersion, attributed to the LDH layer degradation, followed by a gradual increase for prolonged immersion time, attributed to the effect of cerium ions (in accordance with the mechanism described in (3)).

Author Contributions: Conceptualization, M.F. and M.Z.; methodology, M.F. and M.Z.; validation, M.F. and M.Z.; formal analysis, M.Z.; investigation, M.Z.; resources, M.F.; data curation, M.Z.; writing—original draft preparation, M.Z.; writing—review and editing, M.F.; visualization, M.Z.; supervision, M.F.; project administration, M.F.; funding acquisition, M.F. All authors have read and agreed to the published version of the manuscript.

Funding: This research received no external funding.

Institutional Review Board Statement: Not applicable.

Informed Consent Statement: Not applicable.

Data Availability Statement: Data available on request from the corresponding author.

Conflicts of Interest: The authors declare no conflict of interest.

References

- Gigandet, M.P.; Faucheu, J.; Tachez, M. Formation of Black Chromate Conversion Coatings on Pure and Zinc Alloy Electrolytic Deposits: Role of the Main Constituents. *Surf. Coat. Technol.* **1997**, *89*, 285–291. [\[CrossRef\]](#)
- Eppensteiner, F.W.; Jenkins, M.R. Chromate Conversion Coatings. *Met. Finish.* **2000**, *98*, 497–509. [\[CrossRef\]](#)
- Magalhães, A.A.O.; Margarit, I.C.P.; Mattos, O.R. Electrochemical Characterization of Chromate Coatings on Galvanized Steel. *Electrochim. Acta* **1999**, *44*, 4281–4287. [\[CrossRef\]](#)
- Directive 2002/95/EC of the European Parliament and of the Council of 27 January 2003 on the Restriction of the Use of Certain Hazardous Substances in Electrical and Electronic Equipment. Available online: https://ec.europa.eu/environment/topics/waste-and-recycling/rohs-directive_it (accessed on 25 August 2021).
- Wise, J.P.; Wise, S.S.; Holmes, A.L.; LaCerte, C.; Shaffiey, F.; Aboueissa, A.-M. The Cytotoxicity and Genotoxicity of Hexavalent Chromium in Steller Sea Lion Lung Fibroblasts Compared to Human Lung Fibroblasts. *Comp. Biochem. Physiol. Part C Toxicol. Pharmacol.* **2010**, *152*, 91–98. [\[CrossRef\]](#)
- Eivaz Mohammadloo, H.; Sarabi, A.A.; Mohammad Hosseini, R.; Sarayloo, M.; Sameie, H.; Salimi, R. A Comprehensive Study of the Green Hexafluorozirconic Acid-Based Conversion Coating. *Prog. Org. Coat.* **2014**, *77*, 322–330. [\[CrossRef\]](#)
- Khun, N.W.; Frankel, G.S. Composition and Corrosion Protection of Hexafluorozirconic Acid Treatment on Steel: Composition and Corrosion Protection of Hexafluorozirconic Acid. *Mater. Corros.* **2015**, *66*, 1215–1222. [\[CrossRef\]](#)
- Khun, N.W.; Frankel, G.S.; Zimmerman, J. Investigation of Surface Morphology, Wear Resistance, and Adhesiveness of AA6061-T6 Treated in a Hexafluorozirconic Acid-Based Solution. *Corrosion* **2013**, *69*, 259–267. [\[CrossRef\]](#)
- Pinheiro, J.S.; Regio, G.; Cardoso, H.R.P.; Oliveira, C.T.; Ferreira, J.Z. Influence of Concentration and PH of Hexafluorozirconic Acid on Corrosion Resistance of Anodized AA7075-T6. *Mat. Res.* **2019**, *22*, e20190048. [\[CrossRef\]](#)
- George, F.O.; Skeldon, P.; Thompson, G.E. Formation of Zirconium-Based Conversion Coatings on Aluminium and Al–Cu Alloys. *Corros. Sci.* **2012**, *65*, 231–237. [\[CrossRef\]](#)
- Stromberg, C.; Thissen, P.; Klueppel, I.; Fink, N.; Grundmeier, G. Synthesis and Characterisation of Surface Gradient Thin Conversion Films on Zinc Coated Steel. *Electrochim. Acta* **2006**, *52*, 804–815. [\[CrossRef\]](#)
- Verdier, S.; van der Laak, N.; Dalard, F.; Metson, J.; Delalande, S. An Electrochemical and SEM Study of the Mechanism of Formation, Morphology, and Composition of Titanium or Zirconium Fluoride-Based Coatings. *Surf. Coat. Technol.* **2006**, *200*, 2955–2964. [\[CrossRef\]](#)
- Zhong, X.; Wu, X.; Jia, Y.; Liu, Y. Self-Repairing Vanadium–Zirconium Composite Conversion Coating for Aluminum Alloys. *Appl. Surf. Sci.* **2013**, *280*, 489–493. [\[CrossRef\]](#)
- Eivaz Mohammadloo, H.; Sarabi, A.A. Titanium-Phytic Acid Nano Structured Conversion Coating Formation on CRS Substrate. *Prog. Org. Coat.* **2016**, *101*, 391–399. [\[CrossRef\]](#)
- Xia, X.-F.; Gu, Y.-Y.; Xu, S.-A. Titanium Conversion Coatings on the Aluminum Foil AA 8021 Used for Lithium–Ion Battery Package. *Appl. Surf. Sci.* **2017**, *419*, 447–453. [\[CrossRef\]](#)
- Abrashov, A.; Grigoryan, N.; Vagramyan, T.; Asnis, N. On the Mechanism of Formation of Conversion Titanium-Containing Coatings. *Coatings* **2020**, *10*, 328. [\[CrossRef\]](#)
- van Ooij, W.J.; Zhu, D.; Stacy, M.; Seth, A.; Mugada, T.; Gandhi, J.; Puomi, P. Corrosion Protection Properties of Organofunctional Silanes—An Overview. *Tinshhua Sci. Technol.* **2005**, *10*, 639–664. [\[CrossRef\]](#)
- Guglielmi, M. Sol-Gel Coatings on Metals. *J. Sol Gel Sci. Technol.* **1997**, *8*, 443–449. [\[CrossRef\]](#)
- Wang, D.; Bierwagen, G.P. Sol–Gel Coatings on Metals for Corrosion Protection. *Prog. Org. Coat.* **2009**, *64*, 327–338. [\[CrossRef\]](#)
- Figueira, R.B.; Silva, C.J.R.; Pereira, E.V. Organic–Inorganic Hybrid Sol–Gel Coatings for Metal Corrosion Protection: A Review of Recent Progress. *J. Coat. Technol. Res.* **2015**, *12*, 1–35. [\[CrossRef\]](#)
- Chen, W.-K.; Lee, J.-L.; Bai, C.-Y.; Hou, K.-H.; Ger, M.-D. Growth and Characteristics of Cr(III)-Based Conversion Coating on Aluminum Alloy. *J. Taiwan Inst. Chem. Eng.* **2012**, *43*, 989–995. [\[CrossRef\]](#)
- Rosalbino, F.; Scavino, G.; Mortarino, G.; Angelini, E.; Lunazzi, G. EIS Study on the Corrosion Performance of a Cr(III)-Based Conversion Coating on Zinc Galvanized Steel for the Automotive Industry. *J. Solid State Electrochem.* **2011**, *15*, 703–709. [\[CrossRef\]](#)
- Xia, L.; McCreery, R.L. Chemistry of a Chromate Conversion Coating on Aluminum Alloy AA2024-T3 Probed by Vibrational Spectroscopy. *J. Electrochem. Soc.* **1998**, *145*, 3083–3089. [\[CrossRef\]](#)
- Brachetti-Sibaja, S.B.; Domínguez-Crespo, M.A.; Torres-Huerta, A.M.; de la Cruz-Hernández, W.; Onofre-Bustamante, E. Bath Conditions Role in Promoting Corrosion Protection on Aluminum Alloy Using Rare Earth Conversion Coatings. *J. Electrochem. Soc.* **2011**, *159*, C40–C57. [\[CrossRef\]](#)
- Kong, G.; Lingyan, L.; Lu, J.; Che, C.; Zhong, Z. Corrosion Behavior of Lanthanum-Based Conversion Coating Modified with Citric Acid on Hot Dip Galvanized Steel in Aerated 1M NaCl Solution. *Corros. Sci.* **2011**, *53*, 1621–1626. [\[CrossRef\]](#)

26. Wang, C.; Jiang, F.; Wang, F. The Characterization and Corrosion Resistance of Cerium Chemical Conversion Coatings for 304 Stainless Steel. *Corros. Sci.* **2004**, *46*, 75–89. [\[CrossRef\]](#)
27. Hinton, B.R.W.; Arnott, D.R.; Ryan, N.E. The inhibition of aluminium alloy corrosion by cerous cations. In *Metals Forum*; CNRS: Paris, France, 1984; pp. 211–217.
28. Aldykewicz, A.J.; Isaacs, H.S.; Davenport, A.J. The Investigation of Cerium as a Cathodic Inhibitor for Aluminum-Copper Alloys. *J. Electrochem. Soc.* **1995**, *142*, 3342–3350. [\[CrossRef\]](#)
29. Bethencourt, M.; Botana, F.J.; Calvino, J.J.; Marcos, M.; Rodríguez-Chacón, M.A. Lanthanide Compounds as Environmentally-Friendly Corrosion Inhibitors of Aluminium Alloys: A Review. *Corros. Sci.* **1998**, *40*, 1803–1819. [\[CrossRef\]](#)
30. Heller, D.K.; Fahrenholtz, W.G.; O’Keefe, M.J. The Effect of Post-Treatment Time and Temperature on Cerium-Based Conversion Coatings on Al 2024-T3. *Corros. Sci.* **2010**, *52*, 360–368. [\[CrossRef\]](#)
31. Chen, J.; Song, Y.; Shan, D.; Han, E.-H. In Situ Growth of Mg–Al Hydrotalcite Conversion Film on AZ31 Magnesium Alloy. *Corros. Sci.* **2011**, *53*, 3281–3288. [\[CrossRef\]](#)
32. Zhang, F.; Zhao, L.; Chen, H.; Xu, S.; Evans, D.G.; Duan, X. Corrosion Resistance of Superhydrophobic Layered Double Hydroxide Films on Aluminum. *Angew. Chem. Int. Ed.* **2008**, *47*, 2466–2469. [\[CrossRef\]](#)
33. Occelli, M.L.; Robson, H. (Eds.) *Expanded Clays and Other Microporous Solids*; Springer: Boston, MA, USA, 1992; ISBN 978-1-4684-8868-5.
34. Wypych, F.; Satyanarayana, K.G. (Eds.) *Clay Surfaces: Fundamentals and Applications*, 1st ed.; Interface Science and Technology; Elsevier: Amsterdam, The Netherlands; Academic Press: Cambridge, MA, USA, 2004; ISBN 978-0-12-088439-1.
35. Chubar, N.; Gilmour, R.; Gerda, V.; Mičušik, M.; Omastova, M.; Heister, K.; Man, P.; Fraissard, J.; Zaitsev, V. Layered Double Hydroxides as the next Generation Inorganic Anion Exchangers: Synthetic Methods versus Applicability. *Adv. Colloid Interface Sci.* **2017**, *245*, 62–80. [\[CrossRef\]](#)
36. Sokol, D.; Vieira, D.E.L.; Zarkov, A.; Ferreira, M.G.S.; Beganskiene, A.; Rubanik, V.V.; Shilin, A.D.; Kareiva, A.; Salak, A.N. Sonication Accelerated Formation of Mg–Al-Phosphate Layered Double Hydroxide via Sol-Gel Prepared Mixed Metal Oxides. *Sci. Rep.* **2019**, *9*, 10419. [\[CrossRef\]](#)
37. Hibino, T. Anion Selectivity of Layered Double Hydroxides: Effects of Crystallinity and Charge Density: Anion Selectivity of Layered Double Hydroxides: Effects of Crystallinity and Charge Density. *Eur. J. Inorg. Chem.* **2018**, *2018*, 722–730. [\[CrossRef\]](#)
38. Israëli, Y.; Taviot-Guého, C.; Besse, J.-P.; Morel, J.-P.; Morel-Desrosiers, N. Thermodynamics of Anion Exchange on a Chloride-Intercalated Zinc–Aluminum Layered Double Hydroxide: A Microcalorimetric Study. *J. Chem. Soc. Dalton Trans.* **2000**, 791–796. [\[CrossRef\]](#)
39. Costa, D.G.; Rocha, A.B.; Souza, W.F.; Chiaro, S.S.X.; Leitão, A.A. Comparative Structural, Thermodynamic and Electronic Analyses of ZnAlAn– Hydrotalcite-like Compounds (An–Cl–, F–, Br–, OH–, CO₃2– or NO₃–): An Ab Initio Study. *Appl. Clay Sci.* **2012**, *56*, 16–22. [\[CrossRef\]](#)
40. Bouali, A.C.; Serdechnova, M.; Blawert, C.; Tedim, J.; Ferreira, M.G.S.; Zheludkevich, M.L. Layered Double Hydroxides (LDHs) as Functional Materials for the Corrosion Protection of Aluminum Alloys: A Review. *Appl. Mater. Today* **2020**, *21*, 100857. [\[CrossRef\]](#)
41. Iqbal, M.A.; Sun, L.; Barrett, A.T.; Fedel, M. Layered Double Hydroxide Protective Films Developed on Aluminum and Aluminum Alloys: Synthetic Methods and Anti-Corrosion Mechanisms. *Coatings* **2020**, *10*, 428. [\[CrossRef\]](#)
42. Tedim, J.; Kuznetsova, A.; Salak, A.N.; Montemor, F.; Snihirova, D.; Pilz, M.; Zheludkevich, M.L.; Ferreira, M.G.S. Zn–Al Layered Double Hydroxides as Chloride Nanotraps in Active Protective Coatings. *Corros. Sci.* **2012**, *55*, 1–4. [\[CrossRef\]](#)
43. Zhang, C.; Luo, X.; Pan, X.; Liao, L.; Wu, X.; Liu, Y. Self-Healing Li–Al Layered Double Hydroxide Conversion Coating Modified with Aspartic Acid for 6N01 Al Alloy. *Appl. Surf. Sci.* **2017**, *394*, 275–281. [\[CrossRef\]](#)
44. Iqbal, M.A.; Fedel, M. Effect of Synthesis Conditions on the Controlled Growth of MgAl–LDH Corrosion Resistance Film: Structure and Corrosion Resistance Properties. *Coatings* **2019**, *9*, 30. [\[CrossRef\]](#)
45. Iqbal, M.A.; Fedel, M. Effect of Operating Parameters on the Structural Growth of ZnAl Layered Double Hydroxide on AA6082 and Corresponding Corrosion Resistance Properties. *J. Coat Technol. Res.* **2019**, *16*, 1423–1433. [\[CrossRef\]](#)
46. Pang, X.; Sun, M.; Ma, X.; Hou, W. Synthesis of Layered Double Hydroxide Nanosheets by Coprecipitation Using a T-Type Microchannel Reactor. *J. Solid State Chem.* **2014**, *210*, 111–115. [\[CrossRef\]](#)
47. Hu, Y.-L.; Wu, Z.; Zheng, X.; Lin, N.; Yang, Y.; Zuo, J.; Sun, D.; Jiang, C.; Sun, L.; Lin, C.; et al. ZnO/ZnGaNO Heterostructure with Enhanced Photocatalytic Properties Prepared from a LDH Precursor Using a Coprecipitation Method. *J. Alloys Compd.* **2017**, *709*, 42–53. [\[CrossRef\]](#)
48. Zhou, B.; Wei, X.; Wang, Y.; Huang, Q.; Hong, B.; Wei, Y. Effect of Lanthanum Addition on Microstructures and Corrosion Behavior of ZnAl–LDHs Film of 6061 Aluminum Alloys. *Surf. Coat. Technol.* **2019**, *379*, 125056. [\[CrossRef\]](#)
49. Liu, J.; Zhang, Y.; Yu, M.; Li, S.; Xue, B.; Yin, X. Influence of Embedded ZnAlCe–NO₃–Layered Double Hydroxides on the Anticorrosion Properties of Sol–Gel Coatings for Aluminum Alloy. *Prog. Org. Coat.* **2015**, *81*, 93–100. [\[CrossRef\]](#)
50. Qian, Y.; Qiao, P.; Li, L.; Han, H.; Zhang, H.; Chang, G. Hydrothermal Synthesis of Lanthanum-Doped MgAl–Layered Double Hydroxide/Graphene Oxide Hybrid and Its Application as Flame Retardant for Thermoplastic Polyurethane. *Adv. Polym. Technol.* **2020**, *2020*, 1–10. [\[CrossRef\]](#)
51. Pavel, O.D.; Stamate, A.-E.; Zăvoianu, R.; Bucur, I.C.; Bîrjega, R.; Angelescu, E.; Pârvulescu, V.I. Mechano-Chemical versus Co-Precipitation for the Preparation of Y-Modified LDHs for Cyclohexene Oxidation and Claisen-Schmidt Condensations. *Appl. Catal. A Gen.* **2020**, *605*, 117797. [\[CrossRef\]](#)

52. Iqbal, M.A.; Fedel, M. Protective Cerium-Based Layered Double Hydroxides Thin Films Developed on Anodized AA6082. *Adv. Mater. Sci. Eng.* **2020**, 2020, 5785393. [\[CrossRef\]](#)
53. Zhang, G.; Wu, L.; Tang, A.; Ma, Y.; Song, G.-L.; Zheng, D.; Jiang, B.; Atrons, A.; Pan, F. Active Corrosion Protection by a Smart Coating Based on a MgAl-Layered Double Hydroxide on a Cerium-Modified Plasma Electrolytic Oxidation Coating on Mg Alloy AZ31. *Corros. Sci.* **2018**, 139, 370–382. [\[CrossRef\]](#)
54. Abellan, P. The Formation of Cerium(III) Hydroxide Nanoparticles by a Radiation Mediated Increase in Local pH. *RSC Adv.* **2017**, 7, 3831–3837. [\[CrossRef\]](#)
55. Buchheit, R.G.; Mamidipally, S.B.; Schmutz, P.; Guan, H. Active Corrosion Protection in Ce-Modified Hydrotalcite Conversion Coatings. *Corrosion* **2002**, 58, 3–14. [\[CrossRef\]](#)
56. Cullity, B.D.; Stock, S.R. *Elements of X-Ray Diffraction: Pearson New International Edition*, 3rd ed.; Pearson/Prentice Hall: Upper Saddle River, NJ, USA, 2001; ISBN 978-0-201-61091-8.
57. Langford, J.I.; Wilson, A.J.C. Seherer after Sixty Years: A Survey and Some New Results in the Determination of Crystallite Size. *J. Appl. Crystallogr.* **1978**, 11, 102–113. [\[CrossRef\]](#)
58. Aisawa, S.; Hirahara, H.; Uchiyama, H.; Takahashi, S.; Narita, E. Synthesis and Thermal Decomposition of Mn–Al Layered Double Hydroxides. *J. Solid State Chem.* **2002**, 167, 152–159. [\[CrossRef\]](#)
59. Iqbal, M.A.; Fedel, M. Ordering and Disordering of in Situ Grown MgAl-Layered Double Hydroxide and Its Effect on the Structural and Corrosion Resistance Properties. *Int. J. Min. Met. Mater.* **2019**, 26, 1570–1577. [\[CrossRef\]](#)
60. Klopogge, J.T.; Frost, R.L. Fourier Transform Infrared and Raman Spectroscopic Study of the Local Structure of Mg-, Ni-, and Co-Hydrotalcites. *J. Solid State Chem.* **1999**, 146, 506–515. [\[CrossRef\]](#)
61. Zaghouane-Boudiaf, H.; Boutahala, M.; Tiar, C.; Arab, L.; Garin, F. Treatment of 2,4,5-Trichlorophenol by MgAl–SDBS Organo-Layered Double Hydroxides: Kinetic and Equilibrium Studies. *Chem. Eng. J.* **2011**, 173, 36–41. [\[CrossRef\]](#)
62. Wu, Q.; Olafsen, A.; Vistad, Ø.B.; Roots, J.; Norby, P. Delamination and Restacking of a Layered Double Hydroxide with Nitrate as Counter Anion. *J. Mater. Chem.* **2005**, 15, 4695. [\[CrossRef\]](#)
63. Rodrigues, E.; Pereira, P.; Martins, T.; Vargas, F.; Scheller, T.; Correa, J.; Del Nero, J.; Moreira, S.G.C.; Ertel-Ingrisch, W.; De Campos, C.P.; et al. Novel Rare Earth (Ce and La) Hydrotalcite like Material: Synthesis and Characterization. *Mater. Lett.* **2012**, 78, 195–198. [\[CrossRef\]](#)
64. Nakamoto, K. *Infrared and Raman Spectra of Inorganic and Coordination Compounds*, 6th ed.; Wiley: Hoboken, NJ, USA, 2009; ISBN 978-0-471-74339-2.
65. Wu, L.; Yang, D.; Zhang, G.; Zhang, Z.; Zhang, S.; Tang, A.; Pan, F. Fabrication and Characterization of Mg–M Layered Double Hydroxide Films on Anodized Magnesium Alloy AZ31. *Appl. Surf. Sci.* **2018**, 431, 177–186. [\[CrossRef\]](#)
66. Iqbal, M.A.; Sun, L.; Asghar, H.; Fedel, M. Chlorides Entrapment Capability of Various In-Situ Grown NiAl-LDHs: Structural and Corrosion Resistance Properties. *Coatings* **2020**, 10, 384. [\[CrossRef\]](#)
67. Nilchi, A.; Yaftian, M.; Aboulhasanlo, G.; Rasouli Garmarodi, S. Adsorption of Selected Ions on Hydrous Cerium Oxide. *J. Radioanal. Nucl. Chem.* **2009**, 279, 65–74. [\[CrossRef\]](#)
68. Khorsand, S.; Huang, Y. Integrated Casting-Extrusion (ICE) of an AA6082 Aluminium Alloy. In *Light Metals 2017*; Ratvik, A.P., Ed.; The Minerals, Metals & Materials Series; Springer International Publishing: Cham, Switzerland, 2017; pp. 235–241, ISBN 978-3-319-51540-3.
69. Zhang, F.; Liu, Z.-G.; Zeng, R.-C.; Li, S.-Q.; Cui, H.-Z.; Song, L.; Han, E.-H. Corrosion Resistance of Mg–Al-LDH Coating on Magnesium Alloy AZ31. *Surf. Coat. Technol.* **2014**, 258, 1152–1158. [\[CrossRef\]](#)
70. Zhu, B.; Fedel, M.; Andersson, N.-E.; Leisner, P.; Deflorian, F.; Zanella, C. Effect of Si Content and Morphology on Corrosion Resistance of Anodized Cast Al-Si Alloys. *J. Electrochem. Soc.* **2017**, 164, C435–C441. [\[CrossRef\]](#)
71. Wang, F.; Guo, Z. In situ Growth of Durable Superhydrophobic Mg–Al Layered Double Hydroxides Nanoplatelets on Aluminum Alloys for Corrosion Resistance. *J. Alloys Compd.* **2018**, 767, 382–391. [\[CrossRef\]](#)
72. Liang, Z.; Ma, Y.; Li, K.; Liao, Y.; Yang, B.; Liu, L.; Zhu, P. Formation of Layered Double Hydroxides Film on AA2099-T83 Al-Cu-Li Alloy and Its Effect on Corrosion Resistance. *Surf. Coat. Technol.* **2019**, 378, 124967. [\[CrossRef\]](#)
73. Kanoun, O. (Ed.) *Lecture Notes on Impedance Spectroscopy: Measurement, Modeling and Applications. Vol. 4: Includes Selected and Extended Contributions from the International Workshop on Impedance Spectroscopy (IWIS'12)*; CRC Press/Balkema: Boca Raton, FL, USA, 2014; ISBN 978-1-138-00140-4.
74. Jorcin, J.-B.; Orazem, M.E.; Pébère, N.; Tribollet, B. CPE Analysis by Local Electrochemical Impedance Spectroscopy. *Electrochim. Acta* **2006**, 51, 1473–1479. [\[CrossRef\]](#)
75. Scofield, J.H. Comment on “Fractal Model for the Ac Response of a Rough Interface”. *Phys. Rev. Lett.* **1986**, 56, 268. [\[CrossRef\]](#)
76. Dou, B.; Wang, Y.; Zhang, T.; Liu, B.; Shao, Y.; Meng, G.; Wang, F. Growth Behaviors of Layered Double Hydroxide on Microarc Oxidation Film and Anti-Corrosion Performances of the Composite Film. *J. Electrochem. Soc.* **2016**, 163, C917–C927. [\[CrossRef\]](#)